Dynamic instabilities in strongly correlated VSe_2 monolayers and bilayers

Marco Esters,[1] Richard G. Hennig,[2] and David C. Johnson[1,*]
[1]*Department of Chemistry, University of Oregon, Eugene, Oregon 97403, USA*
[2]*Department of Materials Science and Engineering, University of Florida, Gainesville, Florida 32611, USA*
(Received 29 March 2017; revised manuscript received 27 November 2017; published 27 December 2017)

With the emergence of graphene and other two-dimensional (2D) materials, transition-metal dichalcogenides have been investigated intensely as potential 2D materials using experimental and theoretical methods. VSe_2 is an especially interesting material since its bulk modification exhibits a charge-density wave (CDW), the CDW is retained even for few-layer nanosheets, and monolayers of VSe_2 are predicted to be ferromagnetic. In this work, we show that electron correlation has a profound effect on the magnetic properties and dynamic stability of VSe_2 monolayers and bilayers. Including a Hubbard-U term in the density-functional-theory calculations strongly affects the magnetocrystalline anisotropy in the $1T$-VSe_2 structure while leaving the $2H$-polytype virtually unchanged. This demonstrates the importance of electronic correlations for the electrical and magnetic properties of $1T$-VSe_2. The Hubbard-U term changes the dynamic stability and the presence of imaginary modes of ferromagnetic $1T$-VSe_2 while affecting only the amplitudes in the nonmagnetic phase. The Fermi surface of nonmagnetic $1T$-VSe_2 allows for nesting along the CDW vector, but it plays no role in ferromagnetic $1T$-VSe_2. Following the eigenvectors of the soft modes in nonmagnetic $1T$-VSe_2 monolayers yields a CDW structure with a 4×4 supercell and Peierls-type distortion in the atomic positions and electronic structure. The magnetic order indicates the potential for spin-density-wave structures.

DOI: 10.1103/PhysRevB.96.235147

I. INTRODUCTION

The discovery of graphene has sparked heightened interest in studying and finding new two-dimensional (2D) materials [1–3]. Apart from graphene, transition-metal dichalcogenides (TMDs) have been intensely researched as potential candidates as 2D materials due to their layered structures. TMDs exhibit diverse physical and chemical properties, and reducing dimensionality may yield additional properties due to quantum confinement [4]. Additionally, TMDs are chemically diverse, unlike graphene, which is chemically inert. Thus, while functionalization of graphene leads to the loss of some of its properties, functionalizing TMDs can enhance their properties or create new ones [5]. All these factors make 2D TMDs particularly interesting for applications in electronic and sensing devices, and in catalysis and energy storage. As a result, a large amount of research has been done on 2D TMDs using theoretical and experimental methods such as the transition of MoS_2 from an indirect to a direct semiconductor when reducing the dimensions from bulk and multilayers to a monolayer [4–16]. Magnetic 2D materials are especially interesting due to their potential use in spintronic devices [17–23]. The prediction of magnetic TMD materials has been subject to extensive theoretical investigation, such as the systematic change in magnetic properties through strain [18,22,24–27], hydrogenation [27,28], and chemical substitution [29]. Moreover, pristine dichalcogenide monolayers of some first-row transition metals (V, Cr, Mn, Fe) are predicted to have magnetic order [19,20,22,24,26,30–34].

Bulk VSe_2 has been subject to extensive experimental studies due to its ability to intercalate ions [35–39] and its charge-density wave (CDW) [40–46]. Few-layer VSe_2 nanosheets were successfully synthesized using liquid exfoliation [47]. These nanosheets retain the CDW and the metallic properties of its bulk analog, but their magnetic properties were reported to be different: the sheets are ferromagnetic at room temperature, whereas bulk VSe_2 exhibits temperature-independent paramagnetism [48–50]. Isolated monolayers of VSe_2 have not been synthesized yet. However, monolayers of VSe_2 can be found in misfit layer compounds and ferecrystals, where they are sandwiched between monochalcogenides that crystallize in a rocksalt-type structure [51–56]. While the existence of CDWs is well documented in ferecrystals and absent in misfit layer compounds, presumably due to structural distortions, the magnetic properties have not been reported for any of these compounds.

In recent years, density-functional-theory (DFT) calculations were performed on single-layer and few-layer VSe_2, where the V atoms were coordinated in a distorted octahedral [D_{3d}, $1T$-polytype, Fig. 1(a)] and a trigonal prismatic geometry [D_{3h}, $2H$-polytype, Fig. 1(b)] [24,30,34,57]. These calculations predict the ground state of undistorted VSe_2 layers to be the ferromagnetic $2H$-polytype with a metal to semimetal/semiconductor transition when going from the bilayer to the monolayer [30,31,34]. The dynamic stability, an important predictor of a charge-density wave, was not reported. Strong electron correlation may play an important role in monolayer VSe_2. Zhuang and Hennig have shown that the strength of electron correlation affects a variety of properties in VS_2, such as the electronic structure and the stability of the $1T$- and $2H$-polytype [32]. DFT+U calculations by Huang *et al.* on $2H$-VSe_2 monolayers have shown that electron correlation in $2H$-VSe_2 greatly influences the electronic structure [57].

This work presents DFT calculations to explore correlation effects in monolayer and bilayer VSe_2. It will be shown that electron correlation has profound effects on the magnetic properties, electronic structure, and dynamic stability of the $1T$-polytype. First, the van der Waals functionals and the Hubbard-U parameter will be benchmarked against the

*davej@uoregon.edu

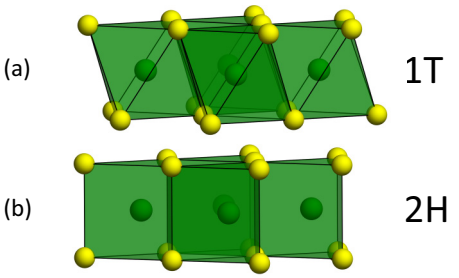

FIG. 1. Structures of monolayer VSe_2 with (a) octahedrally coordinated V as in $1T$-VSe_2 and (b) trigonal-prismatically coordinated V as in the $2H$-VSe_2 polymorph. Vanadium atoms are shown in light yellow and selenium atoms in dark green.

in-plane lattice parameter in ferecrystals. These parameters will be used to determine the magnetic ground state(s) of VSe_2 monolayers and bilayers, and to examine the effect of the Hubbard parameter on the electronic structure. Finally, we will show that VSe_2 is not dynamically stable, and we predict a CDW structure with a Peierls-like distortion and a ferrimagnetic ground state.

II. COMPUTATIONAL METHODS

All DFT calculations were performed using the Vienna ab initio simulation package (VASP) [58–60]. The interactions between the ionic core and the valence electrons were described using the projector-augmented-wave (PAW) method using a cutoff energy of 500 eV [61,62]. The $3p^6 3d^4 s^1$ and the $4s^2 4p^4$ states were used as valence electrons for V and Se, respectively. For the exchange-correlation functional, we compare results for the local-density approximation (LDA) [63], the Perdew-Burke-Ernzerhof (PBE) [64] generalized-gradient approximation (GGA), and the Heyd-Scuseria-Ernzerhof (HSE06) hybrid method with the standard exact-exchange mixing parameter of $\alpha = 0.25$ [65]. For the Hubbard-U term, Dudarev's approach was used to treat localized d orbitals in V, using the effective U parameter, $U_{\text{eff}} = U - J$, with U and J being the on-site Coulomb and exchange parameters, respectively [66]. Since the interactions between individual VSe_2 layers is of van der Waals type, dispersion corrections were included for the GGA functionals using the method of Tkatchenko and Scheffler (TS), Grimme's DFT-D2 method, and Dion's method in the vdW-DF corrected optPBE, optB86b, and optB88 functionals [67–74]. Brillouin-zone integration was carried out using a Γ-centered k-point grid with a high k-point density of approximately 60 k-points per Å^{-1} [75]. Atomic positions and lattice parameters were fully optimized until the forces were smaller than 0.01 eV/Å and the stresses smaller than 0.05 GPa. A vacuum of 30 Å was included for the monolayer and bilayer calculations to minimize interactions between periodic images. For total energy calculations, self-consistency was achieved with an energy convergence of 10^{-6} eV. The magnetic anisotropies were obtained by including spin-orbit interactions in a non-self-consistent calculation using charge and spin densities from calculations without spin-orbit interactions. Since magnetic anisotropies can be in the sub-meV regime, an energy convergence of 10^{-8} eV was used for these calculations. Band structures were visualized and VSe_2 slabs were generated using the open-source PYTHON packages PYMATGEN in conjunction with MPINTERFACES [76,77]. Spin densities were visualized with the program VESTA [78]. Fermi surfaces were calculated using the Wannier interpolation as implemented in the WANNIER90 code and visualized using XCRYSDEN [79,80].

III. RESULTS AND DISCUSSION

A. Stability of undistorted VSe_2 layers with different coordination geometries

Figure 2(a) shows the differences in formation energy, ΔE, between VSe_2 monolayers in the octahedral ($1T$) and trigonal prismatic ($2H$) structure as a function of the Hubbard-U. ΔE depends strongly on the exchange correlation functional, U_{eff}, and the van der Waals functional, similar to the findings for VS_2 [32]. For all functionals, ΔE exhibits a maximum value at intermediate values of U_{eff}. For the GGA functional, PBE and the van der Waals corrected GGA functionals vdW-optPBE, vdW-optB88, vdW-optB86b, TS-GGA, and GGA-D2, the maximum occurs at a lower U_{eff} of 0.5–1.0 eV compared to a U_{eff} of 2.5 eV for the LDA functional. This is similar to the behavior and values observed for VS_2 [32]. For most functionals, the maximum value for ΔE agrees well with the value for HSE06 of 41 meV per formula unit (f.u.), except for the DFT-D2 and the Tkatchenko-Scheffler van der Waals functionals. For the GGA+U methods, the $2H$-structure is stable for U_{eff} below about 2 eV. For the LDA+U method, $1T$ is stable for U_{eff} below 0.5 eV and above 3.5 eV. These trends are similar for the bilayer and the bulk (see Figs. S2 and S3 in the supplemental material [81]). Isaacs and Marianetti attributed these changes in energy for VS_2 to an increased filling and ordering of the V d-orbitals in $1T$-VS_2, and we observe the same trends in the density-matrix elements for VSe_2 [82].

The magnetization m of the $1T$ monolayer as a function of U_{eff} is pictured in Fig. 2(b). The magnetization of the $1T$-polytype is very sensitive to U_{eff}, and for low U_{eff} also to the choice of van der Waals correction. Using the LDA, the magnetization gradually increases until it plateaus at $1.05\mu_B$ at $U_{\text{eff}} = 3.5$ eV. For PBE, the magnetization reaches a maximum of $1.15\mu_B$ at $U_{\text{eff}} = 2.5$ eV and then decreases to unity. While LDA+U shows lower magnetization compared to the HSE06 functional, the magnetization of the GGA+U calculations coincides with HSE06 at $U_{\text{eff}} = 1.5$ eV, regardless of the van der Waals functional. PBE without dispersion correction and the optPBE and optB88 functionals already coincide with HSE06 at $U_{\text{eff}} = 1.0$ eV. For $2H$ (Fig. S1c), the magnetization is at unity using HSE06 and PBE, regardless of U_{eff} and the van der Waals functional, whereas the LDA reaches the same value at $U_{\text{eff}} = 1.5$ eV.

Since isolated monolayers of VSe_2 have not been synthesized yet, finding a good benchmark to decide on an exchange-correlation functional and a value for U_{eff} is challenging. However, ferecrystals contain monolayers of transition-metal dichalcogenides and can be used as an approximation. The compounds $[(MSe)_{1+\delta}]_m[VSe_2]_1$ (M = Pb, Sn) have a relatively constant a-axis lattice parameter of $a = 3.42$ Å,

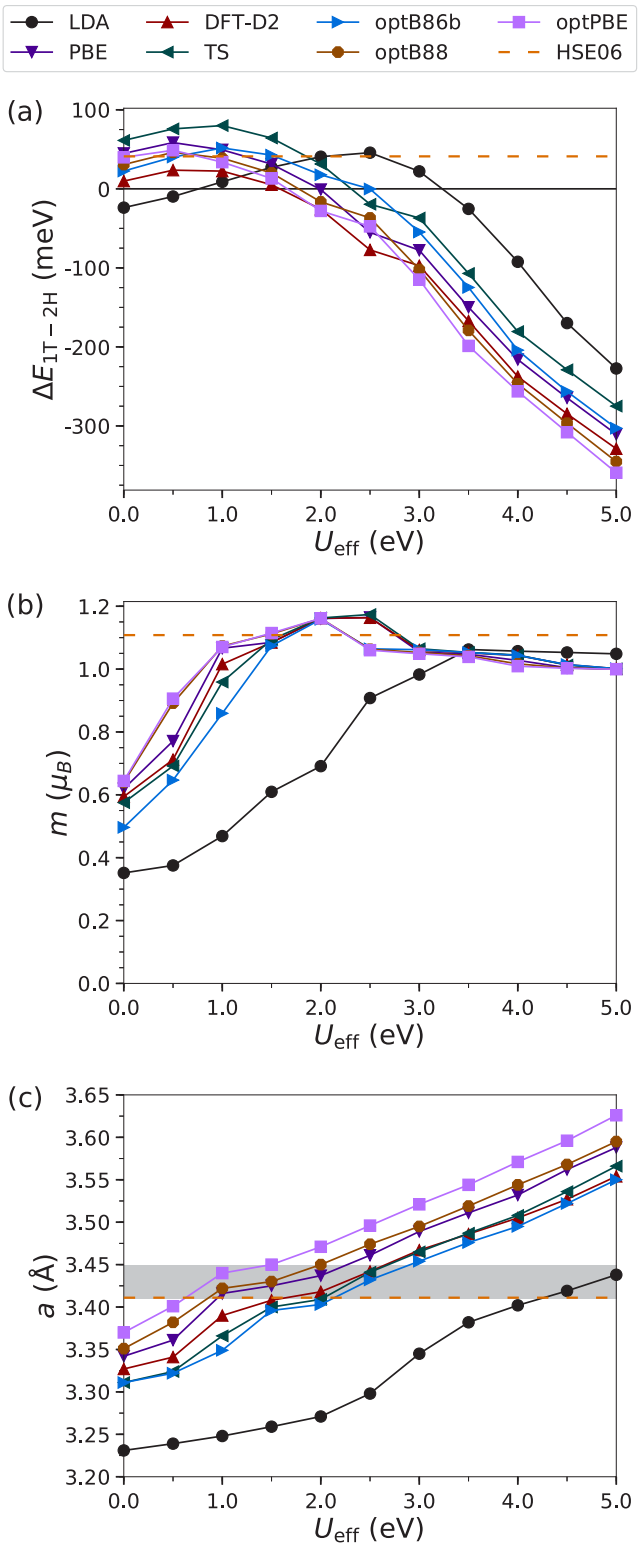

FIG. 2. (a) Energy difference ΔE between $1T$ and $2H$-VSe_2 monolayers as a function of U_{eff}, exchange correlation, and van der Waals functional. Positive ΔE indicates that $2H$ is more stable. (b) Magnetization m of monolayer $1T$-VSe_2 as a function of U_{eff}, exchange correlation, and van der Waals functional. (c) In-plane lattice parameters a of monolayer $1T$-VSe_2. The gray shades represent the range of experimental values found for ferecrystals.

TABLE I. Lattice parameters of the relaxed bulk structure of $1T$-VSe_2 with $U_{eff} = 1.0$ eV using standard PBE, vdW-DF-optPBE, and vdW-DF-optB88 functionals.

	Experiment [48–50]	PBE	optPBE	optB88
a (Å)	3.35	3.42	3.46	3.44
c (Å)	6.10	6.84	6.30	6.13
c/a	1.82	2.00	1.82	1.78

regardless of m, the thickness of the MSe layer [52–56,83]. The in-plane lattice parameter a of the isolated VSe_2 monolayers calculated with different functionals is shown in Fig. 2(c). For all functionals, the a-axis lattice parameter increases with increasing U_{eff}. As the figure shows, adding a Hubbard-U is necessary to reach the experimental in-plane lattice parameter. LDA agrees with experiments only at $U_{eff} = 4.5$ eV. optB86b, DFT-D2, and the Tkatchenko-Scheffler functionals need a moderately high U_{eff} of 2.5 eV, whereas PBE, optPBE, and optB88 only need 1 eV to agree with the experimental lattice parameters. HSE06 underestimates the a-axis lattice parameters only slightly. It is clear that any functional can reproduce these lattice parameters with a high enough value of U_{eff}.

For monolayers, one would expect van der Waals forces to be negligible, and the results should coincide well with the PBE functional without dispersion corrections, which is only true for optPBE and optB88. Since optPBE showed much more stable convergence behavior and also gave a more accurate c/a ratio for the bulk (see Table I), we decided that optPBE with $U_{eff} = 1.0$ eV is the most suitable functional. We cross-checked select results with calculations using the optB86b functional and $U_{eff} = 2.5$ eV, which also reproduces the experimental in-plane geometry well. The strong dependence of the lattice geometry, magnetic properties, and relative phase stability on U_{eff} and the van der Waals functional may indicate that more advanced methods such as dynamic mean-field theory may be necessary to completely describe VSe_2.

It is important to note that PBE predicts bulk $1T$-VSe_2 to be ferromagnetic even though it exhibits temperature-independent paramagnetism in experiments, and should thus converge to a nonmagnetic state. Using mean-field theory, we estimated the Curie temperature of the bulk structure to be approximately 39 and 17 K without a Hubbard-U and with $U_{eff} = 1.0$ eV, respectively, which is significantly below the charge-density transition temperature of 100–110 K (see Table S1 and the corresponding text in the supplemental material [81]) [40–46]. A ferromagnetic ground state is thus not inconsistent with experimental evidence since undistorted $1T$-VSe_2 is not stable in the temperature regime in which it would be ferromagnetic.

B. Magnetic structure of $1T$-VSe_2 and $2H$-VSe_2

There are various configurations of magnetic order possible for the single and bilayer $1T$- and $2H$-polytypes of VSe_2. Figure 3 shows the spin densities for the ferromagnetic (FM)

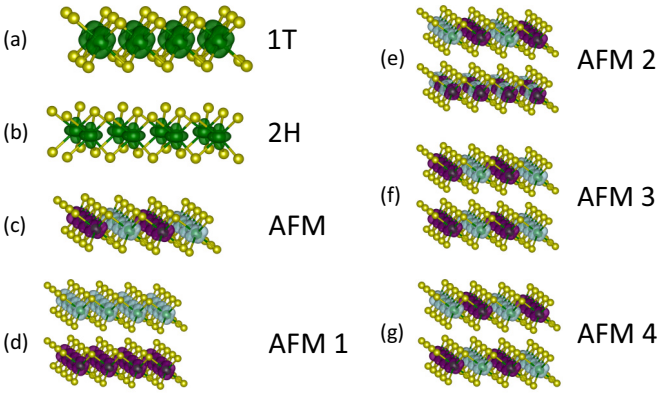

FIG. 3. Spin densities for VSe_2 layers. (a) $1T$-VSe_2 monolayer with ferromagnetic (FM) spin structure. (b) $2H$-VSe_2 monolayer with FM spin structure. (c) $1T$-VSe_2 monolayer with antiferromagnetic (AFM) spin orientation. (d)–(g) $1T$-VSe_2 bilayer with AFM ordering (AFM 1–AFM 4). For $2H$-VSe_2, AFM 3 and AFM 4 are identical. For AFM structures, light red and dark blue spin densities denote opposite spin orientations. The isosurface values are set to $0.01e/a_0^3$, where a_0 is the Bohr radius.

and different antiferromagnetic (AFM) configurations of VSe_2 monolayers and bilayers. For the single-layer polytypes, the striped AFM order in Fig. 3(c) is considered. Four different AFM configurations are considered for the bilayer polytypes and illustrated in Figs. 3(d)–3(g) for the bilayer $1T$-structure. They include configurations of parallel spins in each layer in Fig. 3(d), striped configurations where the stripes are oriented perpendicular in Fig. 3(e), oriented parallel in a staggered pattern in Fig. 3(f), and in an eclipsing pattern in Fig. 3(g). Equivalent patterns are considered for the bilayer $2H$-structure. Due to the different stacking in the $2H$-polytype, the AFM 3 and AFM 4 configurations are identical in $2H$-VSe_2 bilayers.

Table II shows the energies of the various possible types of magnetic order in the single and bilayer $1T$- and $2H$-polytypes ($U_{\text{eff}} = 1.0$ eV). Overall, the magnetic configurations are strongly favored, indicating the tendency of VSe_2 layers to exhibit some form of magnetic order. Similar to the results of Wasey *et al.* using PBE-D2 without a Hubbard-U [31], monolayer VSe_2 is ferromagnetic for both polytypes. As illustrated in Fig. 3, the spin densities around the V atom show a_{1g} symmetry for the $1T$-polytype and a_1' symmetry for the $2H$-polytype (the d_{z^2} orbital). For bilayers, the energy of the antiferromagnetic order with ferromagnetic intralayer (AFM 1) coupling is nearly identical to the ferromagnetic order, whereas the structures with antiferromagnetic intralayer coupling (AFM 2–AFM 4) have substantially higher energies. This suggests that there is a strong intralayer exchange coupling and virtually no interlayer exchange coupling. The magnetic order of VSe_2 multilayers could thus be ferromagnetic or antiferromagnetic, or could show various disordered spin structures along the c axis with ferromagnetic VSe_2 sheets. The AFM energies for $1T$-VSe_2 are substantially lower than for $2H$-VSe_2, suggesting much weaker intralayer exchange coupling in the $1T$-structure.

TABLE II. Energy differences ΔE_{mag} in meV per formula unit with reference to the ferromagnetic order for the nonmagnetic (NM) and antiferromagnetic (AFM) configurations using $U_{\text{eff}} = 1.0$ eV. For the bilayer, four and three different antiferromagnetic cells can be created for the $1T$- and $2H$-polytype, respectively.

	Monolayer		Bilayer				
Polytype	NM	AFM	NM	AFM 1	AFM 2	AFM 3	AFM 4
$1T$	97	25	94	2	25	24	25
$2H$	157	106	148	−1	102	102	–

C. Effect of the electron correlation strength on the electronic structure of VSe_2 layers

Introducing the Hubbard-U parameter has profound effects on the structure of $1T$-VSe_2, whereas the $2H$-polytype remains virtually unaffected. Table III shows the structural and magnetic parameters of the relaxed monolayers and bilayers in their ground states. For $2H$-VSe_2, the lattice parameters increase only slightly by 0.1 Å when U_{eff} is increased to 1.0 eV, and there is no change in lattice parameters when going from the monolayer to the bilayer. The distance between the Se and V planes also remains unchanged, and the magnetization is approximately unity regardless of the Hubbard parameter, the number of layers, and the magnetic structure. For V and Se, the magnitude of the magnetization increases only slightly as well. For $1T$-VSe_2, increasing U_{eff} to 1.0 eV leads to a "flattening" of the monolayer by increasing the in-plane lattice parameter and decreasing the distance between the Se and V planes. For the bilayer, the same trend can be seen, but there is also a small increase in the distance between VSe_2 layers.

The in-plane lattice parameters are in good agreement with the experimental values for ferecrystals, and they are larger than in the bulk [48–56,83]. The magnetization increases significantly from 0.6–0.7μ_B to slightly above unity. This is mostly due to the strong increase of the magnetic moment of the V atom, which almost doubles. Although the magnetic moments of the Se atoms, which are oriented antiparallel to the moments of the V atoms, increase as well, they are much smaller in magnitude. The energy of the $1T$-polytype decreases with respect to the $2H$-polytype, but $2H$ is still the ground state.

The band structures with $U_{\text{eff}} = 1.0$ eV of the ferromagnetic monolayers and bilayers and the AFM 1 bilayer structures are shown in Fig. 4. Ferromagnetic $1T$-VSe_2 is a metal where the Fermi level consists of a minority-spin holelike part centered around the Γ point and a majority-spin electronlike part centered around the M point. Going from the monolayer to the bilayer doubles the number of bands, and the additional bands are degenerate with the bands of the monolayer, except for the highest occupied band near the Γ point, where splitting can be observed. This splitting brings the highest occupied band near the Γ point closer to the Fermi level compared to the monolayer, almost to the same energy as the bands at the K point. This has been observed in other TMDs when transitioning from monolayers to bilayers, and it is due to the introduction of antibonding intralayer interactions [4,8,31,84–86]. Whereas, for example, in MoS_2 this phenomenon leads to a transition from a direct

TABLE III. Comparison of the structural parameters, and magnetic moments for isolated VSe_2 monolayers and bilayers with and without the Hubbard parameter $U_{\text{eff}} = 1.0$ eV. The structural parameters include the in-plane lattice parameter a, the distance between the V and Se planes d(V-Se), and the distance between the two VSe_2 layers in the bilayer $d(VSe_2\text{-}VSe_2)$. The magnetic moments m are given for the unit cell (m_{cell}), and for the contributions from the V and Se atoms m(V) and m(Se), respectively. ΔE denotes the energy difference between the $1T$ and $2H$ polytype (positive when $2H$ is more stable).

Monolayer				
	$U_{\text{eff}} = 0$ eV		$U_{\text{eff}} = 1.0$ eV	
Polytype	$1T$	$2H$	$1T$	$2H$
a (Å)	3.370	3.363	3.441	3.375
d(V-Se) (Å)	1.581	1.606	1.559	1.608
m_{cell} (μ_B)	0.64	1.00	1.07	1.00
m(V) (μ_B)	0.69	1.00	1.27	1.10
m(Se) (μ_B)	−0.05	−0.07	−0.13	−0.10
$\Delta E_{1T\text{-}2H}$ (meV)	39		33	

Bilayer								
	$U_{\text{eff}} = 0$ eV				$U_{\text{eff}} = 1.0$ eV			
Magnetic order	FM		AFM 1		FM		AFM 1	
Polytype	$1T$	$2H$	$1T$	$2H$	$1T$	$2H$	$1T$	$2H$
a (Å)	3.379	3.367	3.376	3.367	3.447	3.378	3.446	3.379
d(V-Se) (Å)	1.582	1.608	1.584	1.609	1.559	1.611	1.560	1.610
	1.574	1.601	1.574	1.601	1.553	1.607	1.554	1.605
$d(VSe_2\text{-}VSe_2)$ (Å)	3.252	3.337	3.245	3.307	3.230	3.393	3.261	3.334
m/f.u. (μ_B)	0.66	0.98	0.00	0.00	1.07	1.00	0.00	0.00
m(V) (μ_B)	0.71	0.99	± 0.68	± 1.01	1.27	1.10	± 1.27	± 1.01
m(Se) (μ_B)	−0.05	−0.07	± 0.05	± 0.07	−0.13	−0.10	± 0.13	± 0.10
$\Delta E_{1T\text{-}2H}$/f.u. (meV)	32		32		22		25	

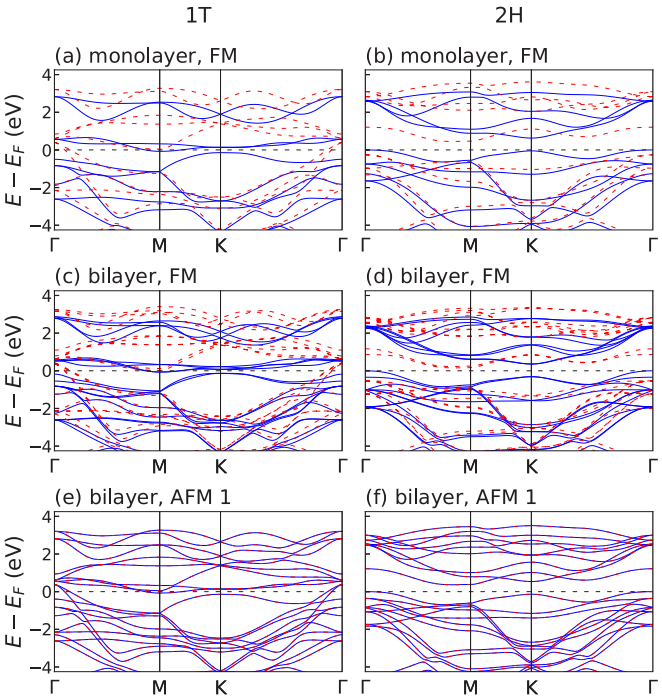

FIG. 4. Spin-polarized band structures for $1T$-VSe_2 (left) and $2H$-VSe_2 (right) layers with $U_{\text{eff}} = 1.0$ eV. (a), (b) Ferromagnetic monolayer; (c), (d) ferromagnetic bilayer; (e), (f) bilayer with AFM 1 structure. Solid blue lines correspond to majority- and red dashed lines to minority-spin bands.

to an indirect semiconductor, the increase in energy is not sufficient to change the electrical properties in $1T$-VSe_2. The band structure of the antiferromagnetic $1T$-VSe_2 bilayer is essentially identical to the sum of two ferromagnetic band structures with opposite spins, providing further evidence that the electronic coupling between individual VSe_2 layers is very small. Similar behavior is observed for the band structures of the $2H$-VSe_2 monolayers and bilayers. The FM $2H$-VSe_2 monolayer is a semiconductor with an indirect gap between Γ and M and a slightly larger direct band gap at the K point. $2H$-VSe_2 remains an indirect semiconductor in the FM bilayer. The transition from semiconductor to metal reported in the literature [31] does not occur when the Hubbard-U is included in the description. Similar to bilayer $1T$-VSe_2, the electronic coupling between the layers in $2H$-VSe_2 layers is very small.

Crystal-field theory predicts that the d orbitals in the $2H$-polytype with D_{3h} symmetry around the V atom split into e' and e'' orbitals, each doubly degenerate, and one a_1' orbital. For the $1T$-polytype, the V atom is coordinated in a D_{3d} symmetry and should split into two sets of doubly degenerate e_g orbitals and one a_{1g} orbital. The orbital-projected band structures of the monolayers in Fig. 5 show this splitting at the Γ point for both polytypes with the energies increasing from e' ($d_{xy} + d_{x^2-y^2}$) to e'' ($d_{xz} + d_{yz}$) and a_1' (d_{z^2}), and from both e_g orbitals ($d_{xy} + d_{x^2-y^2}$) and ($d_{xz} + d_{yz}$) to a_{1g} (d_{z^2}) for $2H$-VSe_2 and $1T$-VSe_2, respectively. Just as in VS_2 [32], the e' and e'' orbitals strongly hybridize with the Se orbitals, whereas the a_1' orbital only hybridizes to a small degree. At the Fermi level, the bands are predominantly of a_1' (Γ point) and e' (K point) character,

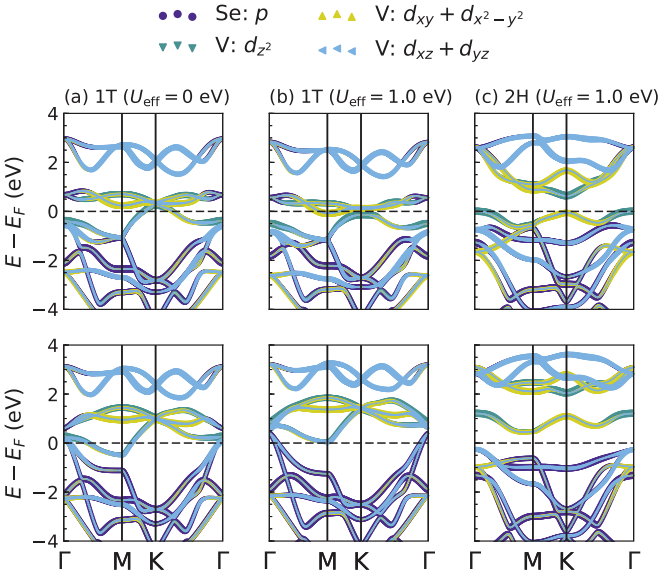

FIG. 5. Orbital resolved majority-spin (top) and minority-spin (bottom) band structures of monolayer VSe_2. (a) $2H$-VSe_2 with $U_{\text{eff}} = 1.0$ eV; (b) $1T$-VSe_2 with $U_{\text{eff}} = 0$ eV; and (c) $1T$-VSe_2 with $U_{\text{eff}} = 1.0$ eV.

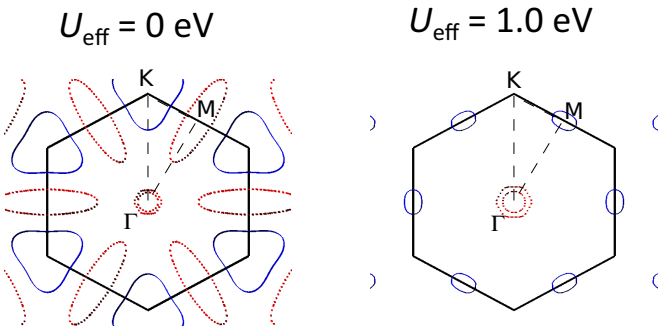

FIG. 6. Fermi surfaces of ferromagnetic $1T$-VSe_2 monolayers for $U_{\text{eff}} = 0$ and 1.0 eV. Solid blue surfaces are from the majority-spin bands and red dashed surfaces are from the minority-spin bands. The edges of the Brillouin zone are shown by black solid lines, and the edges of the irreducible Brillouin zone are shown by black dashed lines.

which is consistent with the shape of the spin density shown in Fig. 3(b) (the e' orbitals are masked by the "ring" of the d_{z^2} orbital). While changes in U_{eff} have only negligible effects on the band structure on the $2H$ polytype, they have strong effects on the band structure of $1T$-VSe_2. Figures 5(a) and 5(b) show that these effects are mostly found at the M and the K point for the majority-spin bands, and at the M point for the minority-spin bands. At the M point, the majority-spin e_g band that consists of the d_{xy} and $d_{x^2-y^2}$ orbitals is lowered in energy and crosses the Fermi level. Near the K point, a majority-spin band with d_{z^2} and partial e_g character crosses the Fermi level for $U_{\text{eff}} = 0$ eV, whereas for $U_{\text{eff}} = 1.0$ eV, the band maximum is shifted below the Fermi level at the K point. This changes the character of the Fermi surface from holelike at K for $U_{\text{eff}} = 0$ eV to electronlike at M for $U_{\text{eff}} = 1.0$ eV. The minority-spin band structures show that at the M point, the e_g band, which is comprised of the V d_{xz} and d_{yz} orbitals, is raised above the Fermi energy. The same band is also raised in energy at the Γ point. Another consequence is that the minority-spin bands that cross the Fermi level near the Γ point are of significantly less e_g character, and remain predominantly of Se p character. At the Γ point, the Se p orbital is also lowered in energy with respect to the e_g and a_{1g} orbitals. This explains the increased magnetization of $1T$-VSe_2 with increased U_{eff}.

These changes can also be observed at the Fermi surfaces (Fig. 6). Without a Hubbard-U, there are Fermi surface pockets around all high-symmetry points. The majority-spin bands form almost triangular-shaped hole pockets around the K point. The surfaces at neighboring K points are almost parallel to each other, which may result in Fermi surface nesting. Fermi surface nesting is often cited as a cause for charge-density waves, but this may not necessarily be the case, as we will discuss in Sec. III D [87,88]. The minority-spin bands form cigar-shaped electron pockets around the M point that point toward the Brillouin zone center where two circular hole pockets of the minority-spin bands can be found. Increasing U_{eff} to 1.0 eV changes the Fermi surface dramatically. The hole pockets at the K point completely disappear, and the cigar-shaped minority-spin electron pockets get replaced by small oval majority-spin electron pockets that point toward the K points. The hole pockets at the Γ point increase in size, but overall, the size of the Fermi surface pockets decreases, reducing the intrinsic carrier concentration of the monolayer. Fermi surface nesting is not possible anymore for $U_{\text{eff}} = 1.0$ eV.

For optB86b and $U_{\text{eff}} = 2.5$ eV (see Fig. S4 in the supplemental material [81]), the energy of the highest occupied majority-spin band decreases further in energy at the K point due to an increased population of the d_{z^2} orbital. In turn, the minority-spin band that is just below the Fermi level at the M point for $U_{\text{eff}} = 0$ eV is now completely above the Fermi energy. This decreases the size of the Fermi surface pockets, showing that the electrical and magnetic properties are sensitive to the value of the Hubbard-U and not just to the structure. The sensitivity of the carrier type and carrier concentration of the different spin channels suggests that not only strain engineering, but also charge screening can be used to tune the electrical and magnetic properties of VSe_2 layers. The latter could be achieved by using a suitable substrate or by incorporating VSe_2 into heterostructures. For example, in the ferecrystalline alloy $[(Sn_{1-x}Bi_xSe)_{1+\delta}][VSe_2]$, the a-axis lattice parameter of the VSe_2 monolayer increases systematically with increasing x, analogous to the trend observed in Fig. 2(c) for increasing U_{eff} [89].

Spin-orbit coupling (SOC) was introduced to determine the magnetocrystalline anisotropy energy (MAE) of the VSe_2 monolayers. The out-of-plane MAE is shown in Fig. 7. Here again, correlation has a strong effect on the $1T$-polytype, whereas the $2H$-polytype is virtually unchanged. Without introducing the Hubbard parameter, $1T$-VSe_2 is nearly isotropic. For $U_{\text{eff}} = 1.0$ eV, however, $1T$-VSe_2 monolayers show a large MAE of about 1.1 meV. This is consistent with the MAE obtained with the optB86b functional and $U_{\text{eff}} = 2.5$ eV, where the MAE was 1.2 meV. For $2H$-VSe_2, the MAE depends only weakly on U_{eff}. It is much smaller than the MAE of

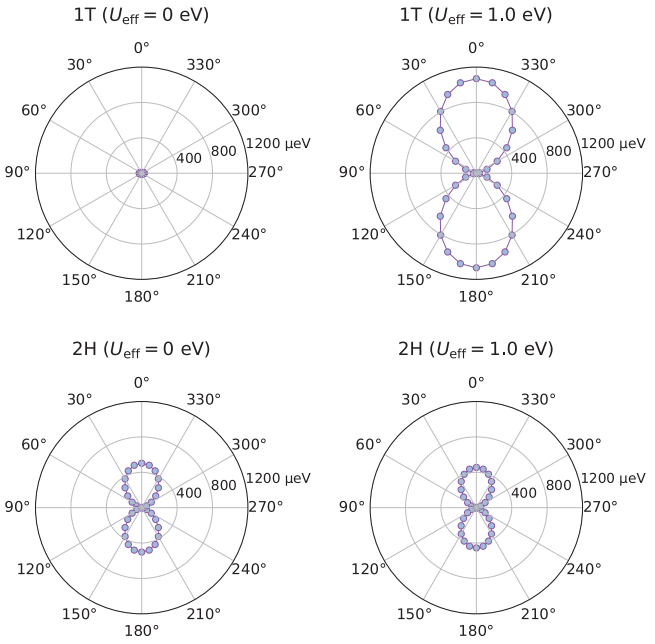

FIG. 7. Angular dependence of the magnetocrystalline anisotropy energy (MAE) with polar angle for monolayer VSe_2. 0° points along the positive z axis.

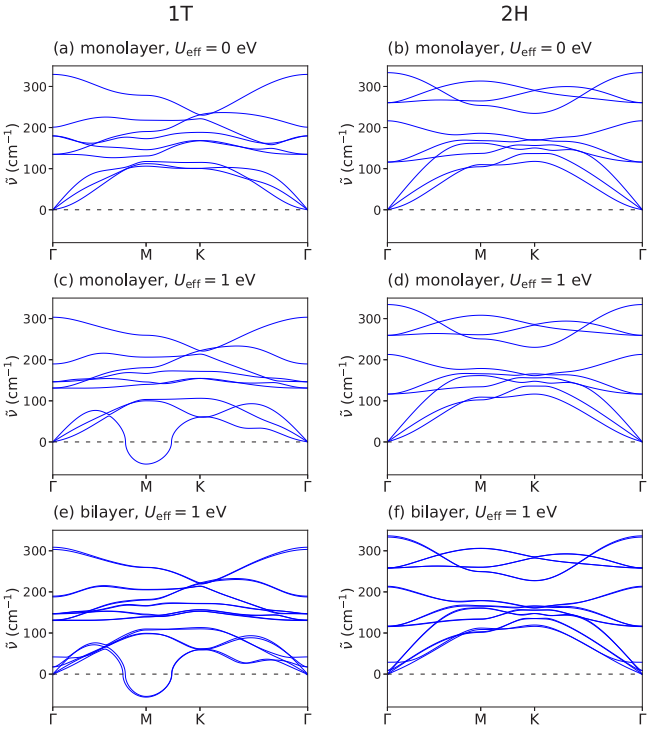

FIG. 8. Phonon-dispersion curves for spin-polarized $1T$-VSe_2 (left) and $2H$-VSe_2 (right) layers. (a), (b) Monolayer with U_{eff} = 0 eV; (c), (d) monolayer with U_{eff} = 1.0 eV; and (e), (f) bilayer with U_{eff} = 1.0 eV.

$1T$-VSe_2 with 0.46 meV. The $1T$ and $2H$ structures both exhibit an easy magnetization plane and belong to the family of XY magnets. This means that a Berezinsky-Kosterlitz-Thouless transition could be observed at a critical temperature that can be estimated from a classical XY model as $T_c = 0.89 J k_B^{-1}$, where J is the exchange integral and k_B is the Boltzmann constant. The exchange integral J can be estimated from the energy difference of the FM and AFM configuration, $\Delta E_{mag} = 8J$ [90]. T_c computes to 137 K for the $2H$-polytype. For the $1T$-polytype, T_c is predicted to be 35 K for optPBE and U_{eff} = 1.0 eV, and 14 K for optB86b and U_{eff} = 2.5 eV (ΔE_{mag} = 11 meV), which is below the experimentally observed charge-density-wave (CDW) transition temperature of 100–110 K (onset) [40–46,52–56]. This means that the magnetic transformation in the $1T$-structure is unlikely to be observable as the $1T$-polytype is unstable at such low temperatures.

D. Dynamic stability of VSe_2 layers

VSe_2 exhibits a charge-density wave in bulk, nanosheets, and ferecrystals. Density-functional perturbation theory (DFPT) as implemented in VASP and the analysis program PHONOPY [91] was used to calculate phonon-dispersion relations for the monolayer and bilayer structures. For these calculations, the structures were relaxed until forces on the ions were below 0.001 Å/s. Phonon-dispersion curves were also calculated for the bulk $1T$-polytype (Fig. S5 in the supplemental material [81]). The soft modes for the bulk agree with the charge-density-wave supercell found in experiments, confirming that our functional choice was reasonable [45,46,92–94].

The phonon-dispersion curves of the ferromagnetic ground states were calculated using a 4×4 supercell and are displayed in Fig. 8. For U_{eff} = 0 eV, the monolayers of VSe_2 are dynamically stable for both polytypes even though the Fermi surface (Fig. 6) allows for nesting, showing that Fermi surface nesting does not necessarily lead to dynamic instabilities. Increasing U_{eff} to 1.0 eV causes imaginary frequencies to appear at the M point for the monolayer of $1T$-VSe_2, whereas the monolayer of $2H$-VSe_2 remains dynamically stable. The dispersion curves for the bilayer are similar to curves for the monolayer, suggesting that the dynamic instabilities in the bilayer have the same origin as in the monolayer. The soft node is at the $\mathbf{q}$ point $(\frac{1}{2},0)$ and its symmetry-equivalent points. The Fermi surface for U_{eff} = 1.0 eV shows no parallel surfaces along a vector that corresponds to these points, so Fermi surface nesting cannot be the cause for these imaginary phonon nodes. The soft mode corresponds to either a 2×1 or 2×2 supercell, which is only half of what was found experimentally for bulk $1T$-VSe_2 [45,46,92–94]. Using optB86b and U_{eff} = 2.5 eV (Fig. S6a in the supplemental material [81]) yields no imaginary phonon modes, which shows that the dynamic stability of spin-polarized $1T$-VSe_2 is sensitive to the value of U_{eff}.

As elaborated in the previous section, the CDW transition temperature for $1T$-VSe_2 is above the predicted magnetic transition temperature, so the structural instabilities may be better described using the nonmagnetic structure. The phonon-dispersion curves of non-spin-polarized VSe_2 layers are shown in Fig. 9. The $1T$ polytype has a soft mode at

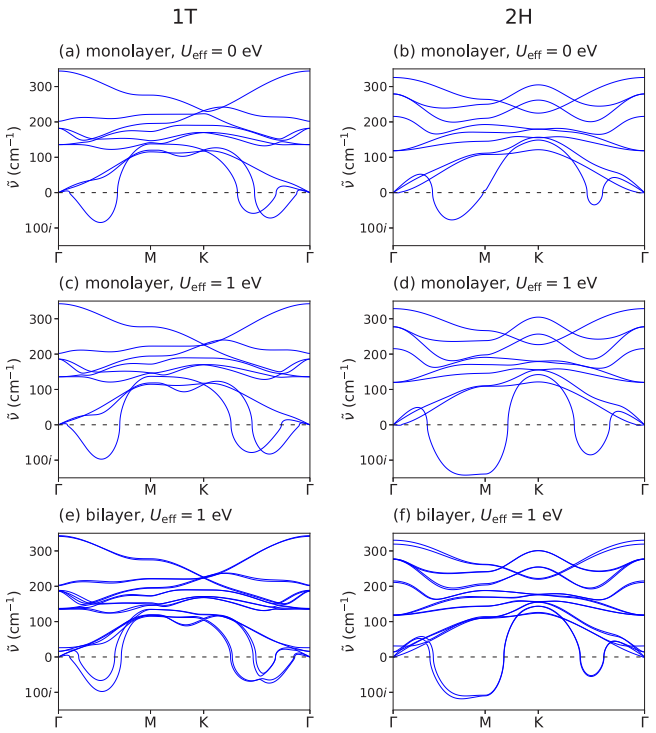

FIG. 9. Phonon-dispersion curves for nonmagnetic $1T$-VSe_2 (left) and $2H$-VSe_2 (right) layers. (a), (b) Monolayer with $U_{\text{eff}} = 0$ eV; (c), (d) monolayer with $U_{\text{eff}} = 1.0$ eV; and (e), (f) bilayer with $U_{\text{eff}} = 1.0$ eV.

$(\frac{1}{4},0)$ (or $\frac{1}{2}M$), which is consistent with a 4×4 supercell as observed for bulk $1T$-VSe_2. Additional phonon modes with lower imaginary frequency appear at $(\frac{1}{6},\frac{1}{6})$ (or $\frac{1}{2}K$) and $(\frac{1}{8},\frac{1}{8})$ (or $\frac{3}{8}K$). The frequencies increase with increasing U_{eff}, indicating that stronger electron localization destabilizes the lattice more. Comparison with optB86b at $U_{\text{eff}} = 2.5$ eV confirms this trend (Fig. S6b). The node at $\frac{1}{2}K$ increases more strongly in frequency with U than the node at $\frac{3}{8}K$, but the node at $\frac{1}{2}M$ remains the strongest. The positions of the soft mode minima are not significantly affected by U_{eff}. The $2H$-polytype is not dynamically stable either with a minimum at $(\frac{1}{3},0)$ $(\frac{2}{3}M)$, suggesting that it distorts into a 3×3 or 3×1 supercell. Adding a Hubbard-U introduces additional instabilities at the M point, resulting in complex phonon spectra. However, since $2H$-VSe_2 has not been synthesized yet and since it is predicted to have a fairly high magnetic transition temperature, it is unknown whether it would undergo this CDW transition from the nonmagnetic state or if it would become ferromagnetic first, in which case it would remain undistorted.

Angle-resolved photoelectron spectroscopy (ARPES) revealed that bulk $1T$-VSe_2 shows partial Fermi surfaces nesting with a nesting vector of $(\frac{1}{4},\frac{1}{4})$ [45,94]. The Fermi surface of nonmagnetic $1T$-VSe_2 monolayers (shown in Fig. 10) is of similar shape as the in-plane Fermi surface determined experimentally for bulk $1T$-VSe_2. Along with the similar phonon spectra, this suggests that the in-plane distortions of the CDW structure are not significantly affected by the dimensionality of VSe_2. Partial nesting can be observed inside the cigarlike electron Fermi surface pockets. The nesting

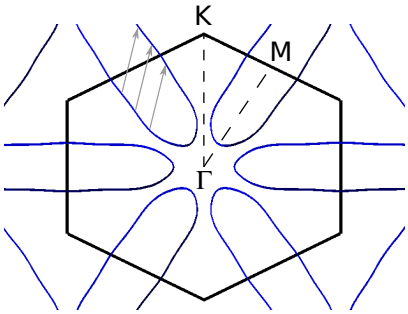

FIG. 10. Fermi surface of a non-spin-polarized $1T$-VSe_2 monolayer. The edges of the Brillouin zone are shown by black solid lines, and the edges of the irreducible Brillouin zone are shown by black dashed lines. Nesting vectors are shown in gray.

vectors (gray arrows in Fig. 10) have the coordinates $(\frac{1}{4},\frac{1}{4})$, which is consistent with the CDW supercell found in bulk and with the soft modes in our phonon spectra. The CDW transition in monolayer $1T$-VSe_2 is thus consistent with a Fermi surface nesting mechanism.

To obtain a possible CDW structure, we followed the eigenvectors of the soft phonon mode. Using the MODULATION tag in PHONOPY, we created distorted structures along the **q** points $(\frac{1}{4},0)$ and $(\frac{1}{4},\frac{1}{4})$, and by using a superposition of the **q** points $(\frac{1}{4},0)$ and $(0,\frac{1}{4})$. The structures were then relaxed using nonmagnetic, ferromagnetic, and antiferromagnetic spin configurations. The most stable structure was found using the superposition and is 82 meV/f.u. more stable than undistorted nonmagnetic $1T$-VSe_2. It has a complex ferrimagnetic order with a total magnetization of approximately $2\mu_B$/cell ($0.12\mu_B$/V atom). The magnetic moments of the individual V atoms are all between $1.05\mu_B$ and $1.25\mu_B$ except for one atom that has a magnetic moment of $0.86\mu_B$. Interestingly, initializing the calculations with both antiferromagnetic and ferromagnetic order led to ferrimagnetic spin order in the final structure.

Figure 11(a) shows the spin densities around the V atoms of the most stable structure. The minority-spin atoms (light blue) form a chain of edge-sharing and corner-sharing triangles. Parallel to this chain, the minority-spin densities form hexagons that are bridged by a single V atom. The V atom inside the hexagon has antiparallel spin and is the atom with the small magnetic moment of $0.86\mu_B$. These structural features can also be observed in the interatomic distances [see Fig. 11(b)]. Inside the chains, most V-V distances are shorter than the a-axis lattice parameter a' of the undistorted nonmagnetic $1T$-VSe_2 monolayer (3.37 Å). The shortest distances (3.19 and 3.24 Å) can be found in triangular clusters inside the majority-spin chains. The chains themselves are spatially separated by at least 3.41 Å. Figure 11(c) shows how these features propagate throughout the crystal. The modulation wavelength in each direction is $4a'$, which is consistent with scanning tunneling microscopy (STM) measurements and the CDW vectors found in ARPES experiments [45,46,92–94].

The in-plane distortions also lead to distorted VSe_6 units. In undistorted VSe_2, the nearest-neighbor V-Se distances are all approximately 2.51 Å. In the distorted structure, only the V atom inside the hexagon has an undistorted coordination

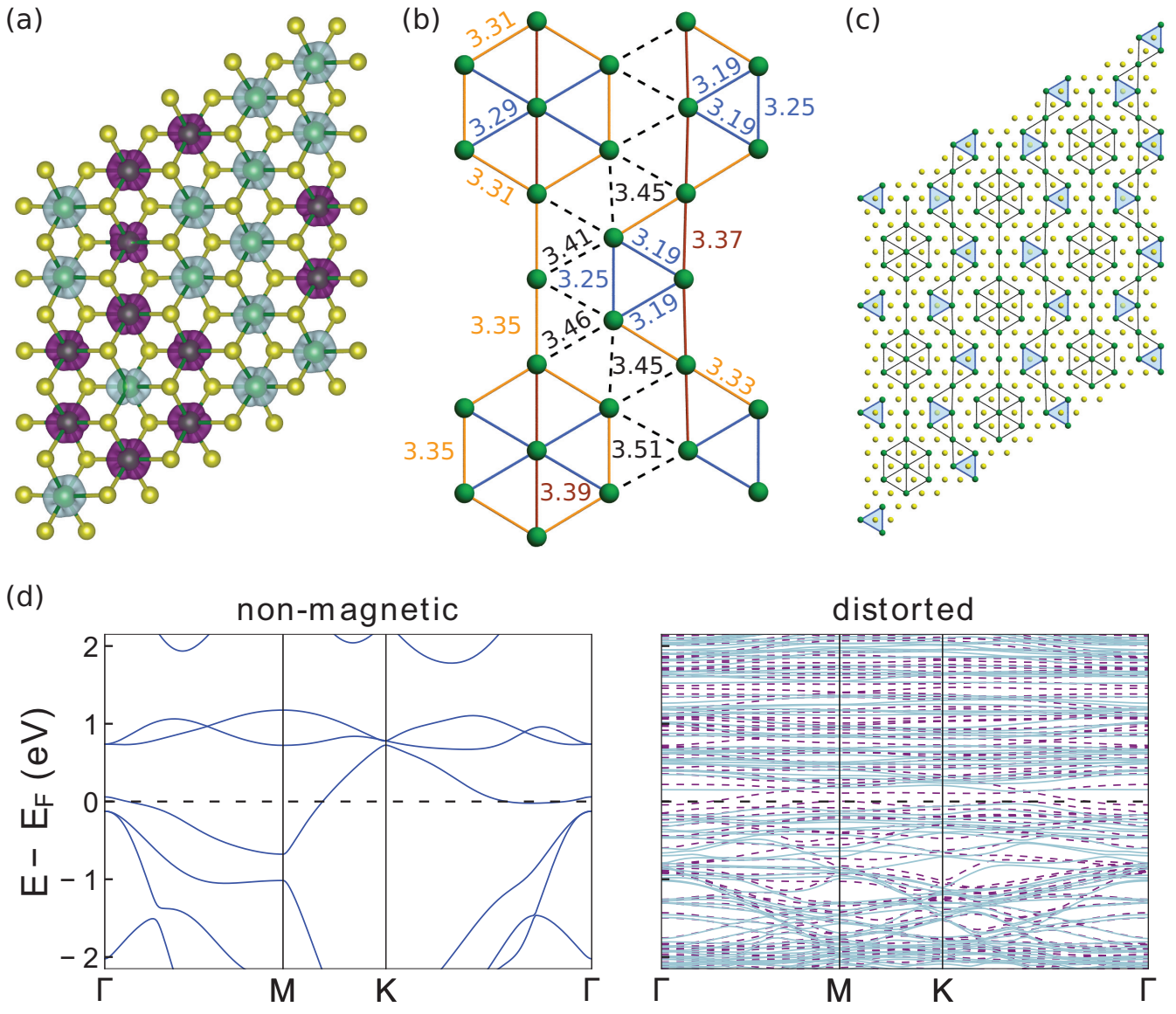

FIG. 11. (a) Unit cell of the most stable distorted structure of monolayer $1T$-VSe_2. The spin densities around the V atoms are shown in light blue and dark purple for the majority and minority spins, respectively. V atoms are dark green and Se atoms are light yellow. The isosurface values are set to $0.01e/a_0^3$, where a_0 is the Bohr radius. (b) Detailed view of the chains of hexagons and triangles with V-V distances given in angstroms. Distances of less than 3.30, 3.35, and 3.40 Å are shown in blue, orange, and brown, respectively. Larger distances are shown by black dashed lines. Se atoms are omitted for clarity. (c) Top view onto a 3×3 supercell of the distorted $1T$-VSe_2 monolayer. Connected V atoms are less than 3.4 Å apart. Small area triangular V clusters are highlighted blue (see the text). (d) Band structures of undistorted nonmagnetic and distorted $1T$-VSe_2 monolayers. For the distorted structure, solid light blue lines represent majority-spin bands and dashed purple lines represent minority-spin bands.

shell, and the spin density around it has the same shape as the V atoms in the antiferromagnetic structures [see Fig. 3(c)]. The coordination shells around the other atoms are strongly distorted, especially around the V atoms in the small triangles and the hexagon corners where V-Se distances as short as 2.48 and as long as 2.56 Å can be found in the same coordination shell. These distortions change the crystal field around the V atoms, which lifts the degeneracy of bands. Figure 11(d) shows the band structures of nonmagnetic and distorted $1T$-VSe_2 monolayers. Nonmagnetic $1T$-VSe_2 is metallic with large electron pockets around the M point. The distorted structure, on the other hand, is a half-metal with small electron pockets near the Γ point in the minority-spin channel. The majority-spin channel shows no Fermi level crossings. This change in the band structure is consistent with electronic transport properties in ferecrystals and in bulk VSe_2 where a sharp increase in the Hall coefficient was observed and attributed to a reduction in carrier concentration without becoming insulating [40,48,49,52,56,83,95]. The periodic structural distortions along with the opening of band gaps indicate a Peierls-type transition at low temperatures.

Comparing the magnetic properties with experimental data is challenging. Apart from the fact that the monolayer may have different magnetic properties than the bulk, the magnetic

properties of bulk $1T$-VSe_2 in the CDW phase are not fully resolved because stoichiometric VSe_2 has not been synthesized yet. In the nonstoichiometric compounds, an increase in the magnetic susceptibility below the CDW transition temperature was observed, and it was discussed whether this increase is due to interstitial V atoms [41,48,49]. Ferrimagnetism or spin-density waves (SDWs) were never considered. The calculated spin densities in Fig. 11(a) suggest that in the monolayer, there is potential for a SDW. For a definitive answer, more experimental data on the magnetic properties in the CDW state are needed. Determining magnetic properties in misfit-layer compounds and ferecrystals containing VSe_2 monolayers and spin-polarized STM measurements on VSe_2 would give crucial information on the spin structure below the CDW transition temperature. Future computational research should focus on SDW structures for further insights into a potential SDW structure.

IV. CONCLUSION AND OUTLOOK

It was shown using density-functional theory including the Hubbard-U parameter that the ground state of two-dimensional $1T$- and $2H$-VSe_2 is ferromagnetic for monolayers, and that for bilayers the ferromagnetic and an antiferromagnetic configuration are energetically nearly degenerate due to weak magnetic interactions between the layers. The VSe_2 monolayers exhibit an easy magnetization plane and belong to the family of XY magnets, but the transition temperature for $1T$-VSe_2 is below the experimentally observed charge-density-wave (CDW) transition temperature. $1T$-VSe_2 displays a charge-density wave in bulk, in few-layer nanosheets, and in ferecrystals. The ferromagnetic monolayers are dynamically stable with the exception of $1T$-VSe_2 for some U_{eff} values. The nonmagnetic layers are unstable with a 4×4 supercell and a 3×3 supercell for the $1T$- and $2H$-polytype, respectively. Within the ab-plane, nonmagnetic $1T$-VSe_2 monolayers show partial Fermi surface nesting similar to the bulk compound. The dynamic instability causes Peierls-type distortions in $1T$-VSe_2 monolayers, which can also be observed in the electronic structure. The magnetic structure of this distorted phase is ferrimagnetic with a very small residual moment and indicates a potential spin-density-wave (SDW) structure. Future research should explore SDW structures in $4 \times 41T$-VSe_2 supercells. However, methods beyond DFT such as dynamical mean-field theory may be necessary to fully describe the properties of VSe_2.

ACKNOWLEDGMENTS

M.E. gratefully acknowledges Joshua Gabriel and Michael Ashton (University of Florida), and Arunima Singh (Lawrence Berkeley National Laboratory) for their assistance with magnetic anisotropy and phonon calculations, and Christian Schön (Max-Planck-Institut für Festkörperforschung in Stuttgart) for helpful discussions. The authors acknowledge the University of Oregon ACISS cluster (National Science Foundation OCI-0960354) and the University of Florida Research Computing system for computing resources. M.E. and D.C.J. acknowledge support from the National Science Foundation under Grant No. DMR-1266217, and R.G.H. acknowledges support from the National Science Foundation under Grant No. DMR-15242776.

[1] K. S. Novoselov, A. K. Geim, S. V. Morozov, D. Jiang, Y. Zhang, S. V. Dubonos, I. V. Grigorieva, and A. A. Firsov, Science **306**, 666 (2004).
[2] K. S. Novoselov, D. Jiang, F. Schedin, T. J. Booth, V. V. Khotkevich, S. V. Morozov, and A. K. Geim, Proc. Natl. Acad. Sci. (USA) **102**, 10451 (2005).
[3] A. Geim and K. Novoselov, Nat. Mater. **6**, 183 (2007).
[4] X. Duan, C. Wang, A. Pan, R. Yu, and X. Duan, Chem. Soc. Rev. **44**, 8859 (2015).
[5] M. Chhowalla, H. S. Shin, G. Eda, L.-J. Li, K. P. Loh, and H. Zhang, Nat. Chem. **5**, 263 (2013).
[6] S. Lebègue and O. Eriksson, Phys. Rev. B **79**, 115409 (2009).
[7] A. Kuc, N. Zibouche, and T. Heine, Phys. Rev. B **83**, 245213 (2011).
[8] D. Xiao, G.-B. Liu, W. Feng, X. Xu, and W. Yao, Phys. Rev. Lett. **108**, 196802 (2012).
[9] H. L. Zhuang and R. G. Hennig, J. Phys. Chem. C **117**, 20440 (2013).
[10] C.-Y. Wang and G.-Y. Guo, J. Phys. Chem. C **119**, 13268 (2015).
[11] H. Wang, H. Yuan, S. Sae Hong, Y. Li, and Y. Cui, Chem. Soc. Rev. **44**, 2664 (2015).
[12] M. Pandey, A. Vojvodic, K. S. Thygesen, and K. W. Jacobsen, J. Phys. Chem. Lett. **6**, 1577 (2015).
[13] D. Voiry, A. Mohite, and M. Chhowalla, Chem. Soc. Rev. **44**, 2702 (2015).
[14] A. E. Maniadaki, G. Kopidakis, and I. N. Remediakis, Solid State Commun. **227**, 33 (2016).
[15] W. Li and J. Li, Nat. Commun. **7**, 10843 (2016).
[16] T. L. Tan, M. F. Ng, and G. Eda, J. Phys. Chem. C **120**, 2501 (2016).
[17] J. Zhou and Q. Sun, J. Am. Chem. Soc. **133**, 15113 (2011).
[18] Y. Zhou, Z. Wang, P. Yang, X. Zu, L. Yang, X. Sun, and F. Gao, ACS Nano **6**, 9727 (2012).
[19] H. Zhang, L.-M. Liu, and W.-M. Lau, J. Mater. Chem. A **1**, 10821 (2013).
[20] M. Kan, J. Zhou, Q. Sun, Y. Kawazoe, and P. Jena, J. Phys. Chem. Lett. **4**, 3382 (2013).
[21] S. Zhang, Y. Li, T. Zhao, and Q. Wang, Sci. Rep. **4**, 5241 (2014).
[22] M. Kan, S. Adhikari, and Q. Sun, Phys. Chem. Chem. Phys. **16**, 4990 (2014).
[23] X. Li and J. Yang, J. Mater. Chem. C **2**, 7071 (2014).
[24] Y. Ma, Y. Dai, M. Guo, C. Niu, Y. Zhu, and B. Huang, ACS Nano **6**, 1695 (2012).
[25] H. Guo, N. Lu, L. Wang, X. Wu, and X. C. Zeng, J. Phys. Chem. C **118**, 7242 (2014).
[26] H. Y. Lv, W. J. Lu, D. F. Shao, Y. Liu, and Y. P. Sun, Phys. Rev. B **92**, 214419 (2015).
[27] P. Manchanda, V. Sharma, H. Yu, D. J. Sellmyer, and R. Skomski, Appl. Phys. Lett. **107**, 032402 (2015).
[28] H. Pan, J. Phys. Chem. C **118**, 13248 (2014).

[29] Y. Zhou, C. Yang, X. Xiang, and X. Zu, Phys. Chem. Chem. Phys. **15**, 14202 (2013).
[30] F. Li, K. Tu, and Z. Chen, J. Phys. Chem. C **118**, 21264 (2014).
[31] A. H. M. A. Wasey, S. Chakrabarty, and G. P. Das, J. Appl. Phys. **117**, 064313 (2015).
[32] H. L. Zhuang and R. G. Hennig, Phys. Rev. B **93**, 054429 (2016).
[33] X. O. Fex, G. Xiang, M. Lan, Y. Nie, D. Yang, and X. Zhang, RSC Adv. **6**, 31758 (2016).
[34] S. Lebègue, T. Björkman, M. Klintenberg, R. M. Nieminen, and O. Eriksson, Phys. Rev. X **3**, 031002 (2013).
[35] A. H. Thompson, J. C. Scanlon, and C. R. Symon, Solid State Ion. **1**, 47 (1980).
[36] H. I. Starnberg, H. E. Brauer, L. J. Holleboom, and H. P. Hughes, Phys. Rev. Lett. **70**, 3111 (1993).
[37] H. E. Brauer, H. I. Starnberg, L. J. Holleboom, and H. P. Hughes, Surf. Sci. **331-333**, 419 (1995).
[38] H. E. Brauer, I. Ekvall, H. Olin, H. I. Starnberg, E. Wahlström, H. P. Hughes, and V. N. Strocov, Phys. Rev. B **55**, 10022 (1997).
[39] I. Ekvall, H. E. Brauer, H. Olin, H. I. Starnberg, and E. Wahlström, Appl. Phys. A **66**, S197 (1998).
[40] A. H. Thompson and B. G. Silbernagel, Phys. Rev. B **19**, 3420 (1979).
[41] L. F. Schneemeyer, A. Stacy, and M. J. Sienko, Inorg. Chem. **19**, 2659 (1980).
[42] B. Giambattista, C. G. Slough, W. W. McNairy, and R. V. Coleman, Phys. Rev. B **41**, 10082 (1990).
[43] G. V. Kamarchuk, A. V. Khotkevich, V. M. Bagatsky, V. G. Ivanov, P. Molinié, A. Leblanc, and E. Faulques, Phys. Rev. B **63**, 073107 (2001).
[44] I. A. Gospodarev, A. V. Eremenko, T. V. Ignatova, G. V. Kamarchuk, I. G. Kolobov, P. A. Minaev, E. S. Syrkin, S. B. Feodosyev, V. D. Fil, A. Soreau-Leblanc, P. Molinie, and E. C. Faulques, Low Temp. Phys. **29**, 151 (2003).
[45] K. Terashima, T. Sato, H. Komatsu, T. Takahashi, N. Maeda, and K. Hayashi, Phys. Rev. B **68**, 155108 (2003).
[46] D. J. Eaglesham, R. L. Withers, and D. M. Bird, J. Phys. C **19**, 359 (1986).
[47] K. Xu, P. Chen, X. Li, C. Wu, Y. Guo, J. Zhao, X. Wu, and Y. Xie, Angew. Chem., Int. Ed. **52**, 10477 (2013).
[48] M. Bayard and M. J. Sienko, J. Solid State Chem. **19**, 325 (1976).
[49] C. F. van Bruggen and C. Haas, Solid State Commun. **20**, 251 (1976).
[50] A. H. Thompson and B. G. Silbernagel, J. Appl. Phys. **49**, 1477 (1978).
[51] G. A. Wiegers, Prog. Solid State Chem. **24**, 1 (1996).
[52] R. Atkins, S. Disch, Z. Jones, I. Häusler, C. Grosse, S. F. Fischer, W. Neumann, P. Zschack, and D. C. Johnson, J. Solid State Chem. **202**, 128 (2013).
[53] R. Atkins, M. Dolgos, A. Fiedler, C. Grosse, S. F. Fischer, S. P. Rudin, and D. C. Johnson, Chem. Mater. **26**, 2862 (2014).
[54] M. B. Alemayehu, M. Falmbigl, K. Ta, J. Ditto, D. L. Medlin, and D. C. Johnson, Angew. Chem., Int. Ed. **54**, 15468 (2015).
[55] M. Falmbigl, D. Putzky, J. Ditto, M. Esters, S. R. Bauers, F. Ronning, and D. C. Johnson, ACS Nano **9**, 8440 (2015).
[56] M. Falmbigl, A. Fiedler, R. E. Atkins, S. F. Fischer, and D. C. Johnson, Nano Lett. **15**, 943 (2015).
[57] P.-R. Huang, Y. He, H. K. Pal, and M. Kindermann, arXiv:1501.00760.
[58] G. Kresse and J. Hafner, Phys. Rev. B **49**, 14251 (1994).
[59] G. Kresse and J. Furthmüller, Comput. Mater. Sci. **6**, 15 (1996).
[60] G. Kresse and J. Furthmüller, Phys. Rev. B **54**, 11169 (1996).
[61] P. E. Blöchl, Phys. Rev. B **50**, 17953 (1994).
[62] G. Kresse and D. Joubert, Phys. Rev. B **59**, 1758 (1999).
[63] J. P. Perdew and A. Zunger, Phys. Rev. B **23**, 5048 (1981).
[64] J. P. Perdew, K. Burke, and M. Ernzerhof, Phys. Rev. Lett. **77**, 3865 (1996).
[65] J. Heyd, G. E. Scuseria, and M. Ernzerhof, J. Chem. Phys. **118**, 8207 (2003).
[66] S. L. Dudarev, G. A. Botton, S. Y. Savrasov, C. J. Humphreys, and A. P. Sutton, Phys. Rev. B **57**, 1505 (1998).
[67] A. Tkatchenko and M. Scheffler, Phys. Rev. Lett. **102**, 073005 (2009).
[68] A. Tkatchenko, R. A. DiStasio, R. Car, and M. Scheffler, Phys. Rev. Lett. **108**, 236402 (2012).
[69] S. Grimme, J. Comput. Chem. **27**, 1787 (2006).
[70] T. Bučko, J. Hafner, S. Lebègue, and J. G. Ángyán, J. Phys. Chem. A **114**, 11814 (2010).
[71] M. Dion, H. Rydberg, E. Schröder, D. C. Langreth, and B. I. Lundqvist, Phys. Rev. Lett. **92**, 246401 (2004).
[72] G. Román-Pérez and J. M. Soler, Phys. Rev. Lett. **103**, 096102 (2009).
[73] J. Klimeš, D. R. Bowler, and A. Michaelides, J. Phys.: Condens. Matter **22**, 022201 (2010).
[74] J. Klimeš, D. R. Bowler, and A. Michaelides, Phys. Rev. B **83**, 195131 (2011).
[75] H. J. Monkhorst and J. D. Pack, Phys. Rev. B **13**, 5188 (1976).
[76] S. P. Ong, W. D. Richards, A. Jain, G. Hautier, M. Kocher, S. Cholia, D. Gunter, V. L. Chevrier, K. A. Persson, and G. Ceder, Comput. Mater. Sci. **68**, 314 (2013).
[77] K. Mathew, A. K. Singh, J. J. Gabriel, K. Choudhary, S. B. Sinnott, A. V. Davydov, F. Tavazza, and R. G. Hennig, Comput. Mater. Sci. **122**, 183 (2016).
[78] K. Momma and F. Izumi, J. Appl. Crystallogr. **44**, 1272 (2011).
[79] A. A. Mostofi, J. R. Yates, G. Pizzi, Y.-S. Lee, I. Souza, D. Vanderbilt, and N. Marzari, Comput. Phys. Commun. **185**, 2309 (2014).
[80] A. Kokalj, Comput. Mater. Sci. **28**, 155 (2003).
[81] See the Supplemental Material at http://link.aps.org/supplemental/10.1103/PhysRevB.96.235147 for the U_{eff} dependence of the total energies, magnetizations, and a-axis lattice parameters for 1T- and 2H-VSe_2 in monolayers, bilayers, and bulk, for the optB86b band structure, and results of select bulk calculations, which includes Ref. [96].
[82] E. B. Isaacs and C. A. Marianetti, Phys. Rev. B **94**, 035120 (2016).
[83] O. K. Hite, M. Falmbigl, M. B. Alemayehu, M. Esters, S. R. Wood, and D. C. Johnson, Chem. Mater. **29**, 5646 (2017).
[84] H. Schmidt, F. Giustiniano, and G. Eda, Chem. Soc. Rev. **44**, 7715 (2015).
[85] Y. Zhang, T.-R. Chang, B. Zhou, Y.-T. Cui, H. Yan, Z. Liu, F. Schmitt, J. Lee, R. Moore, Y. Chen, H. Lin, H.-T. Jeng, S.-K. Mo, Z. Hussain, A. Bansil, and Z.-X. Shen, Nat. Nanotechnol. **9**, 111 (2014).
[86] A. Splendiani, L. Sun, Y. Zhang, T. Li, J. Kim, C. Y. Chim, G. Galli, and F. Wang, Nano Lett. **10**, 1271 (2010).
[87] M. H. Whangbo and E. Canadell, J. Am. Chem. Soc. **114**, 9587 (1992).
[88] M. Calandra, I. I. Mazin, and F. Mauri, Phys. Rev. B **80**, 241108(R) (2009).

[89] M. Falmbigl, Z. Hay, J. Ditto, G. Mitchson, and D. C. Johnson, J. Mater. Chem. C **3**, 12308 (2015).
[90] J. F. Fernández, M. F. Ferreira, and J. Stankiewicz, Phys. Rev. B **34**, 292 (1986).
[91] A. Togo and I. Tanaka, Scr. Mater. **108**, 1 (2015).
[92] H. P. Hughes, C. Webb, and P. M. Williams, J. Phys. C **13**, 1125 (1980).
[93] J.-J. Kim, C. Park, and H. Olin, J. Korean Phy. Soc. **31**, 713 (1997).
[94] V. N. Strocov, M. Shi, M. Kobayashi, C. Monney, X. Wang, J. Krempasky, T. Schmitt, L. Patthey, H. Berger, and P. Blaha, Phys. Rev. Lett. **109**, 086401 (2012).
[95] C. S. Yadav and A. K. Rastogi, Solid State Commun. **150**, 648 (2010).
[96] D. Zhang, J. Ha, H. Baek, Y.-H. Chan, F. D. Natterer, A. F. Myers, J. D. Schumacher, W. G. Cullen, A. V. Davydov, Y. Kuk, M. Y. Chou, N. B. Zhitenev, and J. A. Stroscio, Phys. Rev. Mater. **1**, 024005 (2017).